Supplementary Materials for

Flexible Single Crystal Silicon Nanomembrane Photonic Crystal Cavity

Xiaochuan Xu,[1,2,, ‡] Harish Subbaraman,[2, ‡] Swapnajit Chakravarty,[2] Amir Hosseini,[2] John Covey,[1] Yalin Yu,[3] David Kwong,[1] Yang Zhang,[1] Wei-Cheng Lai,[1] Yi Zou,[1] Nanshu Lu,[3] and Ray T. Chen[1,*]*

correspondence to: xiaochuan.xu@utexas.edu
raychen@uts.cc.utexas.edu

This PDF file includes:

Materials and Methods
Figure S1 to S10
Table S1
Caption for Movie S1

Other Supplementary Materials for this manuscript includes the following:

Movie S1

Materials and Methods

1. Device Fabrication

The device is fabricated on commercially available silicon-on-insulator (SOI) with 250 nm single crystal silicon device layer, 3 μm buried oxide (BOX) layer, and 675 μm silicon handle, as shown in Figure S1a. The wafer is cleaved into 2 cm×2 cm chips, and the chips are cleaned through piranha bath. Hexamethyldisilazane (HMDS) is spin coated at 4000 rpm for 35s to enhance the adhesion between electron beam resist and silicon. Electron beam resist ZEP520a is spin coated at 6000 rpm for 35s, giving a resist of 350 nm thickness. The pattern is transferred onto the resist by JBL 6000 (Figure S1b), and then to the silicon layer through reactive ion etching (HBr/Cl_2), as shown in Figure S1c. The resist is stripped off by PG remover and piranha bath.

2. Transfer Procedure

The transfer process is illustrated in Figure S2. As shown in Figure S2a, the Kapton film is cleaned with acetone and methanol, and dried with compressed nitrogen gas. To make chip handling and bonding easier, the Kapton film is mounted on a rigid substrate, such as a silicon chip. A layer of 2 μm thick SU-8 is spin casted on the Kapton film and baked at 90°C for 20 minutes. The SOI chip with fabricated L13 cavities is cleaned by piranha bath. The native oxide is removed by 1:6 buffered oxide etchant (BOE). A layer of 2 μm SU-8 is spin coated and also baked at 90°C for 20 minutes. The extended baking time assures a complete evaporation of the solvent, which is crucial to a successful bonding. Besides, SU-8 has extraordinary self-planarization capability at a temperature above its glass transition temperature (64 °C), [1, 2] and thus long term baking minimizes the edge bead effect as well as other thickness variations.[2]

SU-8 is an acid-catalyzed polymer.[3] Its crosslink relies on the generation of Lewis acid through ultra-violet (UV) exposure. Since neither Kapton nor SOI is transparent to UV light, it is impossible to cure SU-8 after bonding. The conventional bonding procedure is to cure SU-8 prior to bonding and let it reflow above its glass transition temperature, which is around 180 °C, depending on its crosslink level. However, since silicon, SU-8, and Kapton have distinct coefficients of thermal expansion (CTE), the stack could crack during the thermal cycle involving high temperature. SU-8 is a chemical amplified resist. One photon produces a photoproduct that in turn induces hundreds of reactions. Therefore, the SU-8 layer on Kapton is partially cured before bonding, while the SU-8 on SOI remains uncured. The partially cured SU-8 provides Lewis acid to initiate crosslinking and the uncured SU-8 serves as a buffer layer, which reflows at low temperature. The bonding pressure is applied through a home-made bonder (Figure S3). The sample is mounted between two thick Pyrex glass slides. The steel ball and the Belleville washer spreads the point force generated by the thumb screw onto the thick Pyrex glass plate. This structure forms a gradient pressure distribution with higher pressure at the center and lower at the edges. This distribution prevents the formation of air cavities in between the two SU-8 layers. The applied pressure reduces as SU-8 reflows, which can be compensated by the thermal expansion of the Belleville washers. The sample is kept in a 90 °C oven for 12 hours to allow for polymer to reflow and to squeeze out the trapped air bubbles.

After bonding, the silicon handle is removed by deep reactive ion etch (DRIE), as described in Figs. S2c and S2d. DRIE generates a large amount of heat, so the carrier wafer on which the sample sits is kept at ~ 15 °C through Helium flow underneath. However, the thermal conductivities of SU-8 and Kapton are merely 0.2 W/mK and 0.52 W/mK, respectively, and thus the heat generated by the etching process cannot be dissipated fast enough. Consequently, a significant temperature gradient builds up between the top surface and the bottom of the rigid

substrate, subjecting the sample to cracking. The CTE mismatch further aggravates this issue. To control the thermal budget, the silicon handle is mechanically polished to ~100 μm, as shown in Figure S2c, to shorten the etching time. The etching recipe is also carefully optimized to accommodate the thermal requirements. The conventional Bosch process contains three steps: polymer deposition, polymer etching, and silicon etching. The polymer deposition time is set to 5s to protect the perimeter of the membrane, because the charges accumulated on the Kapton surface bend the electric field and etch silicon and SU-8 from the side. As the quality of the perimeter of silicon nanomembrane is not important, the anisotropic polymer etching step is removed in this application. The polymer is removed during the silicon etching step. The inductively coupled plasma (ICP) power is carefully tuned to keep it slightly above the threshold of maintaining plasma to reduce heat generation. This adjustment sacrifices the etch rate. To compensate it, a long silicon etching time of 30s is used in each cycle. The etch rate of this recipe is around 2.7 μm/cycle with a selectivity of ~80:1 over silicon dioxide. The 3 μm BOX is therefore used as a stopping layer to protect the SiNM underneath, and it can be removed by hydrofluoric (HF) acid etching afterwards.

Before removing the BOX layer, photoresist is applied on both the bottom and the top of the sample except the BOX region for protection. Because HF attacks Kapton/SU-8 bonds and SU-8/silicon bonds, a few droplets of HF are applied on the BOX directly instead of immersing the whole sample into HF solution to prevent the delamination of the silicon nanomembrane. The surface tension of the silicon dioxide constrains the solution within the SiNM. The drawback is that etching speed decreases as the HF concentration decreases. Thus, a few more drops of HF needs to be added to maintain sufficient HF concentration. The process is shown in Figure S2e. After transfer, the thickness of the SU-8 is measured to be around 3 μm. The thickness variation across the entire chip is ~200 nm, due to gradient bonding pressure. The holes of the photonic crystal structures are filled with SU-8 which reduces the sensitivity of the photonic crystal cavity. Another reactive ion etching step is used to remove the SU-8 inside the holes, as shown in Figure S2f. Finally, the Kapton film is peeled off from the silicon carrier, as shown in Figure S2g. The sample after transfer is shown in Figure S4. It can be seen that the transferred devices can be bent beyond the limit of their rigid counterparts without breaking or cracking.

3. Grating Coupler Design and Characterization

Coupling light into and out from the transferred devices is very challenging. End-fire coupling is a straight forward option but not a feasible one for flexible silicon photonic devices. First the facet is extremely difficult to prepare due to the soft nature of the substrate, [4] which turns the simple solution into a disaster. Moreover, the coupling efficiency is close to zero via direct butt coupling due to the large mode mismatch. An alternative solution is grating couplers. However, conventional grating couplers require multiple lithography and etching steps to reduce the index contrast and increase directionality.[5-7] Besides, the one dimension periodic structure is not mechanically strong enough for flexible devices. Subwavelength grating (SWG) couplers provide a viable option.[8, 9] The low index region of SWG couplers is comprised of artificial nanostructures, which are more robust. The entire grating can be fabricated together with other photonic components with efficiency comparable to those that demand multiple lithography and alignment steps.[5-7] Since the holes of SWG couplers could be completely filled or partially filled with SU-8, the grating coupler needs to work properly in both situations.

Figure 5a shows the schematic of the SWG coupler. A complete study of the SWG coupler requires three dimension (3D) simulations. The simulation time would be prohibitively long. To simplify the simulation, we treat the subwavelength structures as a uniform material because the

subwavelength period is much smaller than the wavelength inside the waveguide according to effective medium theory (EMT).[9-11] So the 3D problem can be simplified into 2D. In addition, the reflection of bottom cladding can be ignored because the SU-8 layer is very thick, and the index contrast between SU-8 (1.575) and Kapton (1.79) is much smaller than that between silicon dioxide (1.45) and silicon (3.476). The simulation and optimization procedure is similar to reference [8], so it would not be reiterated here. The optimized subwavelength refractive index $n_{sub}$is 2.45. The grating period Λ is 0.69 μm. An example of the fabricated grating coupler is shown in Figure S5b. The 2D finite-difference-time-domain (FDTD) simulation of fiber to grating coupling is shown by the red curve in Figure S5c. The coupling angle is ~9.4°. The grating has a theoretical coupling efficiency of -3.2 dB. The transmission spectrum of the grating coupler after transfer is shown in the same figure (blue curve). The grating coupler demonstrates a coupling efficiency of -4.4 dB at 1536.7 nm, and a 3 dB bandwidth of 50 nm. The discrepancy of the measured coupling efficiency and the peak wavelength from the simulated values is caused by the dimension variation induced by the transfer process. When the holes are infiltrated with SU-8, the refractive index of the subwavelength structure increases to 2.92. As a result, the peak wavelength shifts to 1585 nm, and the peak efficiency reduces to -6.2dB even when the fiber is tilted to 20°, according to the simulation result shown by the red curve in Figure S5d. However, the experimental results demonstrate a better efficiency of -5.2 dB, and the peak wavelength shifts back to 1545 nm. It is possibly due to the fact that the holes of subwavelength structures become larger when they are filled with SU-8, which leads to a smaller effective refractive index and therefore the peak wavelength shifts to shorter wavelengths. To sum up, the grating demonstrates satisfying performance with and without SU-8 fillings. Although the peak wavelength shifts about 30 nm, the wavelength range of interest is still covered due to the large bandwidth of the grating coupler.

To assure the grating is functional while being bent, the performance of the grating coupler under different bending conditions is also characterized, as shown in Figure S6. The sample under investigation is the grating filled with SU-8. The input and output fibers are tilted at a fixed angle of 20°. Figure S6a shows the shift of peak wavelength under bending along longitudinal direction. For longitudinal face-out (LFO) bending, the peak wavelength shifts to longer wavelength, while for longitudinal face-in (LFI) bending the peak wavelength shifts to shorter wavelength. It is experimentally observed that the efficiency of grating couplers is not affected by bending. Since the coupling efficiency heavily depends upon the effective index, a relatively stable coupling efficiency indicates that the subwavelength structure has negligible deformation, otherwise the coupling efficiency should show significant decrease. This assertion matches the mechanical simulation, which shows that the maximum strain is around 1%, corresponding to only about 7 nm variation in the period. Thus, we can assume that the shift of the peak wavelength is mainly caused by the change of the relative coupling angle. As shown by the cartoon in Figure S6a, the coupling angle reduces along with the bending radius. According to the phase matching condition:

$$\frac{2\pi n_{neffavg}}{\lambda} = \frac{2\pi n_c \sin\theta_o}{\lambda} + \frac{2\pi}{\Lambda} \tag{S-1}$$

The peak wavelength $\lambda_0$can be calculated by:

$$\lambda_0 = \Lambda\left(n_{neffavg} - n_c \sin\theta_o\right) \tag{S-2}$$

Here, Λ is the grating period. $n_{neffavg}$ is the average effective index of the grating coupler. n_c is the refractive index of the cladding, which equals to 1. θ_0 represents the fiber tilting angle, which can be estimated by approximately considering the bending curvature as part of a circle. The red curves in Figure S6b and c are the simulation results, which matches the experimental data. Similarly, for transverse face-out (TFO) and transverse face-in (TFI) bending, shown in Figure S6d~e, the peak wavelength of the grating coupler stays the same due to the fact that the bending does not change any of the parameters in the phase matching condition. The discrepancy is from the fact that the device cannot be precisely placed on the top of the curvature.

4. Mechanical Analysis

As mechanics and photonics have different conventions on coordinates, to avoid potential ambiguities, the coordinate system needs to be clarified prior to analysis. In this paper, we define the light propagation direction as z axis. In the device plane, the direction perpendicular to the light propagation direction is defined as x axis. The out of plane direction is y axis. The device is fabricated along <110> crystal direction, and thus x and z axis are along <110> crystal direction and y axis is along <100> crystal direction.

As indicated by Figure S7a, the film comprises of three layers, a 250 nm thick silicon device layer, a ~3 μm thick SU-8 layer, and a 125 μm thick Kapton film. Conducting a complete analysis on the mechanical and optical properties of the deformed photonic crystal cavity in 3D space demands unrealistically long time. Alternatively, we first exploit plane strain model in the yz plane for longitudinal bending (or xz plane for transverse bending) to estimate the bending-induced strain of the silicon nanomembrane, and then use plane stress model in the xz plane with prescribed strain boundary condition obtained from the bending analysis to simulate the deformation of the photonic crystal cavity.

Subjecting the film to a compressive force causes it buckle (Figure S7b) and the bent shape can be described by the following sinusoidal curve: [12, 13]

$$w = w_0 \sin\left(\frac{\pi D}{L - \Delta L}\right) \tag{S-3}$$

w_0 is the deflection of the specimen at the center of the specimen. It is defined as:

$$w_0 = \frac{2}{\pi} L \sqrt{\frac{\Delta L}{L} - \frac{\pi^2 h^2}{12 L^2}} \tag{S-4}$$

D=z for bending along z direction (longitudinal bending), and D=x for bending along x direction (transverse bending). $w$and h denote the deflection of the specimen in y direction and the total thickness of the specimen (a summation of the thickness of the silicon layer h_1, the thickness of the SU-8 layer h_2, and the thickness of the Kapton film h_3), respectively. The second term under the square root can be dropped because h (125 μm) is much smaller than the length of the specimen L (30 mm). The bending radius at the center of the specimen can be estimated by: [12]

$$R = \frac{L}{2\pi\sqrt{\frac{\Delta L}{L}}} \tag{S-5}$$

The strain on the top surface can be calculated by dividing its distance to the neutral plane by the bending radius. The position of the neutral plane can be calculated through [14]:

$$d = \frac{\sum_{i=1}^{3} \overline{E_i} h_i d_i}{\sum_{i=1}^{3} \overline{E_i} h_i} \tag{S-6}$$

Here, $\bar{E}_i = E_i/(1-v_i^2)$, representing the plane strain modulus. E_i is the Young's modulus, and v_i is Poisson's ratio. h_i denotes the thickness of the i-th layer. The Young's moduli and Poisson's ratios of the involved materials are listed in Table S1. d_i is the distance between the middle plane of the i-th layer to the bottom of the specimen as denoted in Figure S7A. It has been proved that patterned silicon nanomembranes bonded to Kapton substrates have very similar strains (excluding the edge effect) to their blanket counterpart because of the small elastic mismatch [15]. Since the patterned area is very small and the microcavities only cover a small fraction of the area, the effective Young's modulus of the patterned nanomembrane can be assumed to be close to the Young's modulus of silicon. On the top surface, the strain in the bending direction γ_{bend} can be calculated by:

$$\gamma_{bend} = \frac{h-d}{R} \tag{S-7}.$$

The relation between the bending radius and the strain is illustrated by the curve shown in Figure S8. Eq. (S-7) implies that the strain of silicon nanomembrane could be tuned by adjusting the position of the neutral plane. For example, when $h = d$, the strain induced by bending is negligible and the film could be bended to an extremely small curvature.

The strain γ_{bend} calculated from (S-7) is applied in the 2D plane stress finite element modeling by specifying displacement boundary conditions at the left and right ends. For longitudinal bending (bending in z direction), $\gamma_{zz} = \gamma_{bend}$; for transverse bending (bending in x direction), $\gamma_{xx} = \gamma_{bend}$. Since the dimension of the cavity is much smaller than the bending radius, and also the light propagates along the bending curvature, the in-plane 2D stretching and compressing is a close approximation to bending in 3D space. The deformation of the holes is simulated by finite-element-method (FEM) using commercial software COMSOL. Due to the nonuniformly distributed holes, the stress distribution is not uniform. Hence, here, an averaged stress over the whole 2D domain is used for the finite-difference time-domain (FDTD) simulations.

5. Bending Induced Photo-elastic Effect

As indicated in Figure S8, bending can induce more than 1% of strain, which corresponds to stress as high as one GPa. The refractive index change caused by stress is larger than 0.01.[16] According to reference [17], a small perturbation of the refractive index is sufficient to cause a shift

of the resonance as the mode is confined inside the high index silicon nanomembrane. The frequency shift Δf could be evaluated by

$$\Delta f = \left(\frac{1}{1+\frac{\eta \Delta n}{n}} - 1 \right) f_0 \tag{S-8}$$

for small index change $\Delta n/n$. η is the fraction of mode field confined inside the high index region. f_0 represents the resonance frequency. Assuming η equals to 0.85, a change of 0.01 could result in a resonance wavelength shift of around 4 nm. Thus, the photo-elastic effect must be taken into consideration.

In our specific case, the strain could be written as: [18]

$$\gamma = \begin{pmatrix} \gamma_{xx} & \gamma_{xy} & \gamma_{xz} \\ \gamma_{xy} & \gamma_{yy} & \gamma_{yz} \\ \gamma_{xz} & \gamma_{yz} & \gamma_{zz} \end{pmatrix} \tag{S-9}$$

Due to the symmetry, there are six independent elements. Since the shear force has negligible effects on the optical performance, γ_{xy}, γ_{xz}, and γ_{yz} can be ignored. [16] Thus, the strain tensor is simplified into

$$\gamma = \begin{pmatrix} \gamma_{xx} & 0 & 0 \\ 0 & \gamma_{yy} & 0 \\ 0 & 0 & \gamma_{zz} \end{pmatrix} \tag{S-10}$$

The dielectric tensor takes the form of [18]

$$\varepsilon = \begin{pmatrix} n_{xx}^2 & n_{xy}^2 & n_{xz}^2 \\ n_{xy}^2 & n_{yy}^2 & n_{yz}^2 \\ n_{xz}^2 & n_{yz}^2 & n_{zz}^2 \end{pmatrix} \tag{S-11}$$

For cubic crystals like silicon, the dielectric tensor can be simplified into:

$$\varepsilon = \begin{pmatrix} n_{xx}^2 & 0 & 0 \\ 0 & n_{yy}^2 & 0 \\ 0 & 0 & n_{zz}^2 \end{pmatrix} \tag{S-12}$$

This strain-optic coefficient of this type of crystal can be written as [16] :

$$p=\begin{pmatrix} p_{11} & p_{12} & p_{12} & 0 & 0 & 0 \\ p_{12} & p_{11} & p_{12} & 0 & 0 & 0 \\ p_{12} & p_{12} & p_{11} & 0 & 0 & 0 \\ 0 & 0 & 0 & p_{44} & 0 & 0 \\ 0 & 0 & 0 & 0 & p_{44} & 0 \\ 0 & 0 & 0 & 0 & 0 & p_{44} \end{pmatrix} \tag{S-13}$$

For silicon, p_{11}=-0.101, and p_{12}=0.0094. The relation between the refractive index and the strain is governed by:

$$\Delta\begin{pmatrix} 1/n_{xx}^2 \\ 1/n_{yy}^2 \\ 1/n_{zz}^2 \\ 1/n_{yz}^2 \\ 1/n_{xz}^2 \\ 1/n_{xy}^2 \end{pmatrix}=\begin{pmatrix} p_{11} & p_{12} & p_{12} & 0 & 0 & 0 \\ p_{12} & p_{11} & p_{12} & 0 & 0 & 0 \\ p_{12} & p_{12} & p_{11} & 0 & 0 & 0 \\ 0 & 0 & 0 & p_{44} & 0 & 0 \\ 0 & 0 & 0 & 0 & p_{44} & 0 \\ 0 & 0 & 0 & 0 & 0 & p_{44} \end{pmatrix}\begin{pmatrix} \gamma_{xx} \\ \gamma_{yy} \\ \gamma_{zz} \\ 0 \\ 0 \\ 0 \end{pmatrix} \tag{S-14}$$

Obviously, $\Delta(1/n_{yz}^2)$, $\Delta(1/n_{xz}^2)$, and $\Delta(1/n_{xy}^2)$ are zero due to the fact that the shear strain has been ignored in the discussion. Therefore, the equation turns into

$$\Delta\begin{pmatrix} 1/n_{xx}^2 \\ 1/n_{yy}^2 \\ 1/n_{zz}^2 \end{pmatrix}=\begin{pmatrix} p_{11} & p_{12} & p_{12} \\ p_{12} & p_{11} & p_{12} \\ p_{12} & p_{12} & p_{11} \end{pmatrix}\begin{pmatrix} \gamma_{xx} \\ \gamma_{yy} \\ \gamma_{zz} \end{pmatrix} \tag{S-15}$$

With the stress-strain relation: [19]

$$\gamma_{xx}=\frac{1}{E_{xx}}[\sigma_{xx}-\nu(\sigma_{yy}+\sigma_{zz})] \tag{S-16}$$

$$\gamma_{yy}=\frac{1}{E_{yy}}[\sigma_{yy}-\nu(\sigma_{xx}+\sigma_{zz})] \tag{S-17}$$

$$\gamma_{yy}=\frac{1}{E_{yy}}[\sigma_{yy}-\nu(\sigma_{xx}+\sigma_{zz})] \tag{S-18}$$

The relation between the stress and refractive index is:

$$\begin{pmatrix} n_{xx} \\ n_{yy} \\ n_{zz} \end{pmatrix}=\begin{pmatrix} n_0 \\ n_0 \\ n_0 \end{pmatrix}-\begin{pmatrix} C_1 & C_2 & C_2 \\ C_2 & C_1 & C_2 \\ C_2 & C_2 & C_1 \end{pmatrix}\begin{pmatrix} \sigma_{xx} \\ \sigma_{yy} \\ \sigma_{zz} \end{pmatrix} \tag{S-19}$$

Here,

$$C_1 = \frac{n_0^3}{2}\left[\frac{p_{11}}{E_{xx}} - \frac{p_{12}}{E_{yy}}\upsilon - \frac{p_{12}}{E_{zz}}\upsilon\right] \quad \text{(S-20)}$$

$$C_2 = \frac{n_0^3}{2}\left[-\frac{p_{11}}{E_{xx}}\upsilon + \frac{p_{12}}{E_{yy}} - \frac{p_{12}}{E_{zz}}\upsilon\right] \quad \text{(S-21)}$$

C_1 and C_2 are -13.3×10^{-12} Pa^{-1} and 4.7×10^{-12} Pa^{-1}, respectively. The average stress and induced change of refractive index are shown in Figure S9. The average stress versus strain, and refractive index versus strain appears to have a linear correlation.

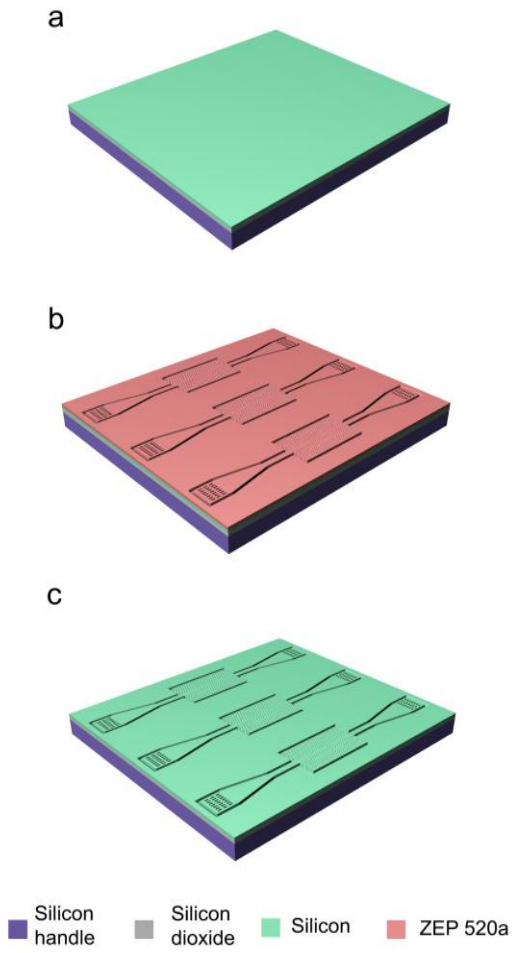

Figure S1.

Pattern SOI into L13 Cavity. a. SOI chip with 250 nm silicon, 3 μm BOX and 675 μm silicon handle. b. Pattern electron beam resist layer. c. Transfer the pattern onto silicon device layer with RIE.

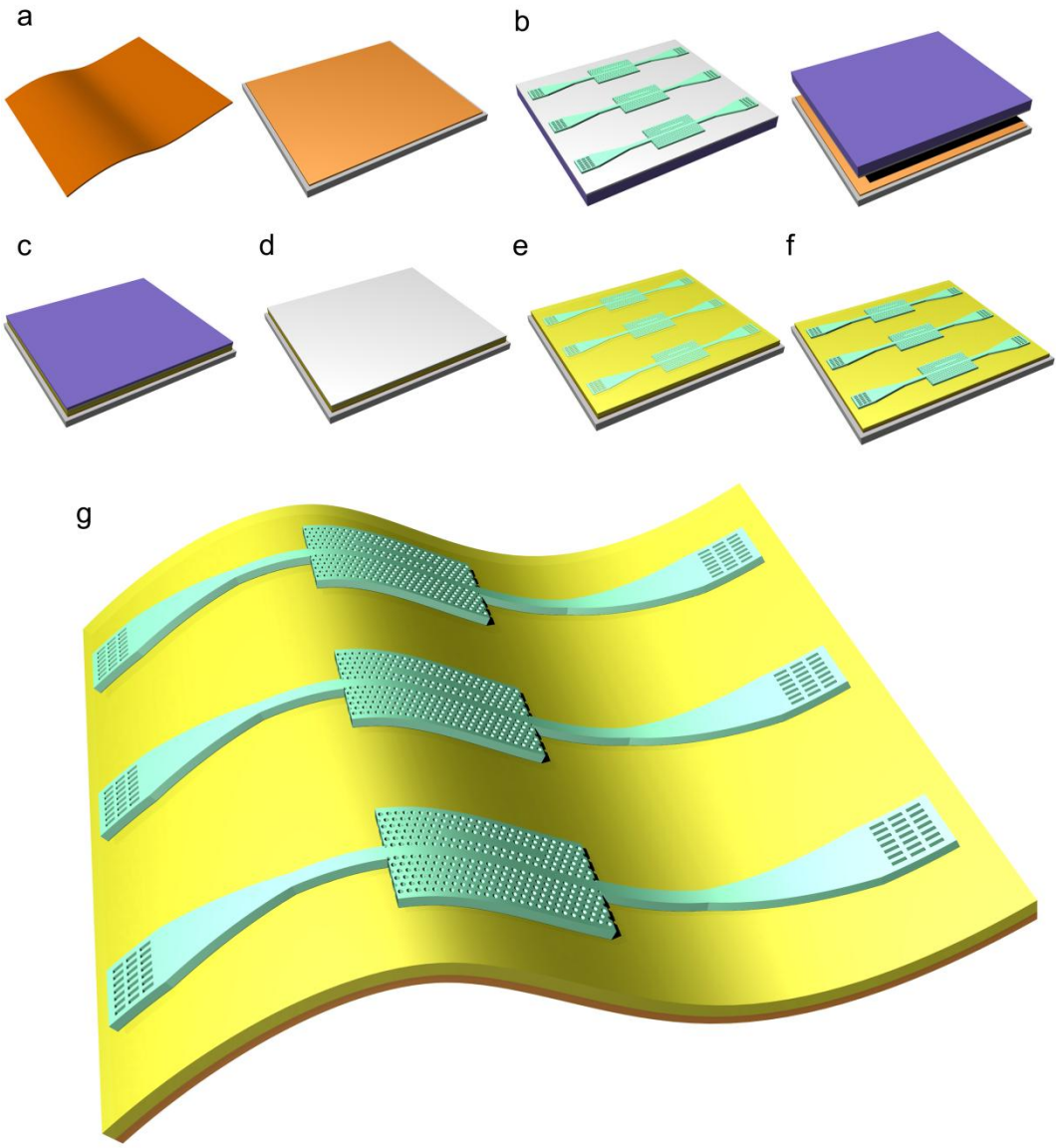

Figure S2

Tranfer Process. a. Clean and mount a Kapton film on a silicon chip. b. Fabricate L13 PC microcavity devices with integrated SWG couplers on SOI, flip over and bond the chip onto the Kapton film with SU-8 as adhesive layer. c. Thin down the silicon handle to ~ 100 μm using mechanical polishing. d. Use deep silicon etching to etch away the remaining ~ 100 μm silicon. e. Remove the box layer with HF. f. Remove the SU 8 filled into the holes of photonic crystal to enhance the sensitivity. g. Peel off the Kapton film.

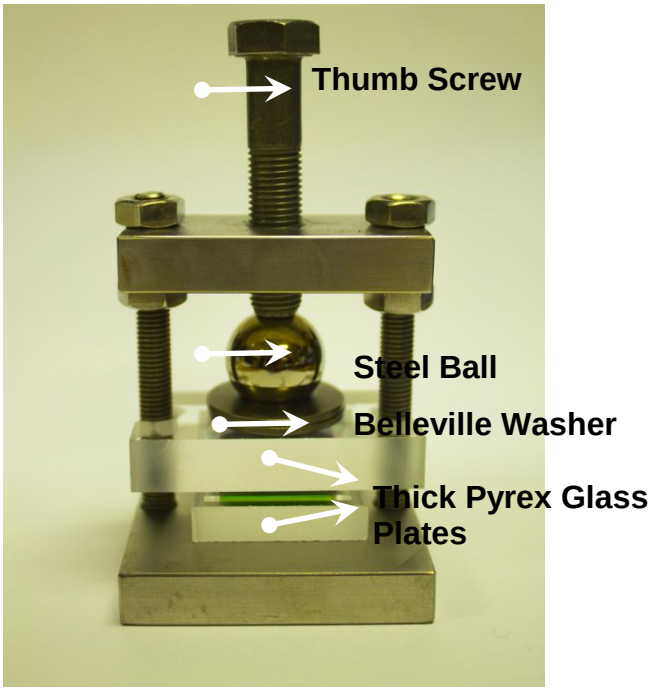

Figure S3

The home-made bonder. The samples to be bonded are mounted between two thick Pyrex glass plates. The pressure is controlled via a thumb screw, a steel ball and Belleville washer.

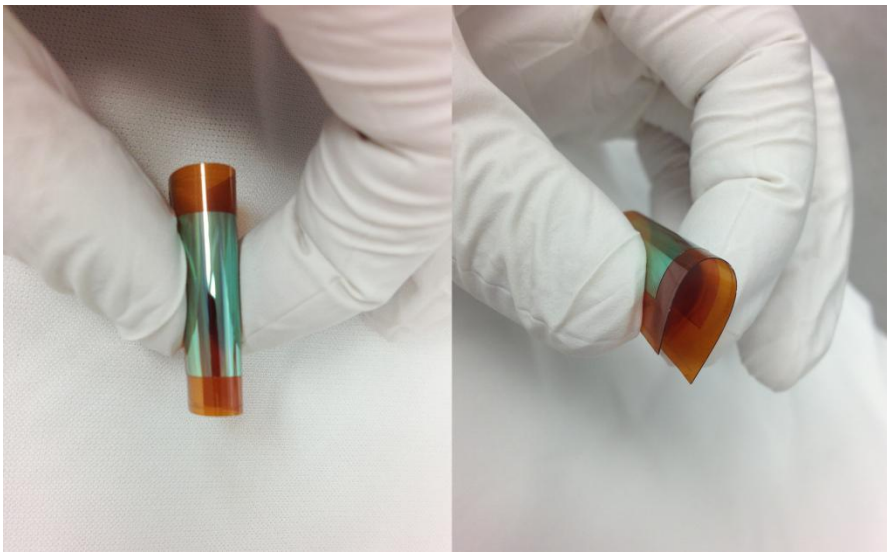

Figure S4

Silicon nanomembrane transferred onto Kapton film. The transferred nanomembrane can be bent to a very small radius without breaking or cracking the film.

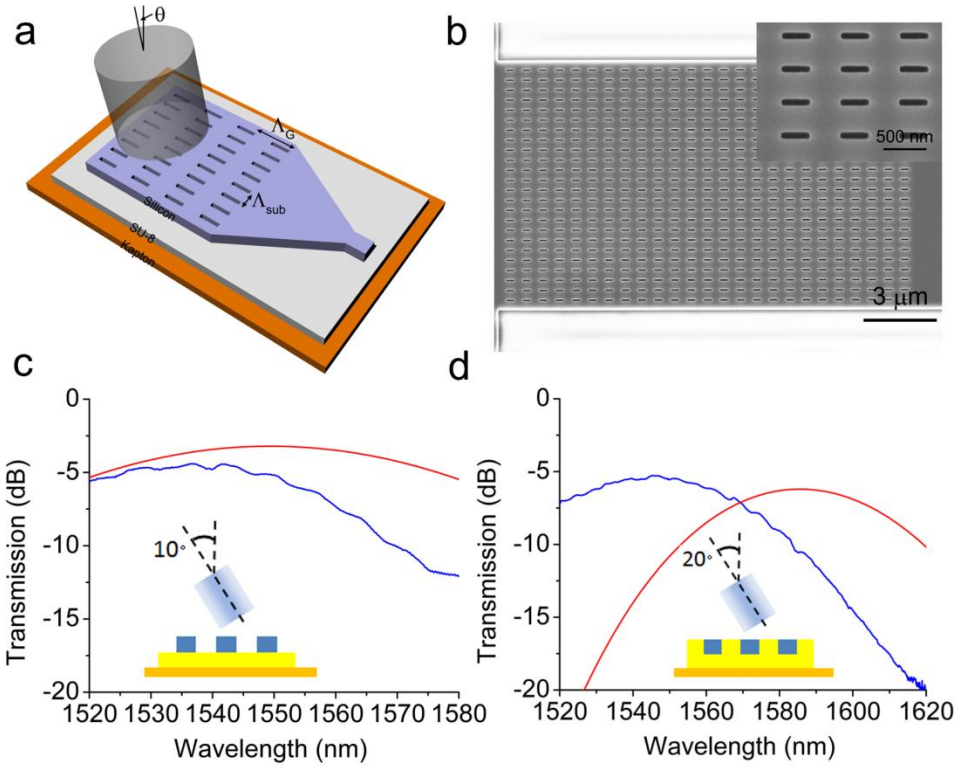

Figure S5

a. schematic of the subwavelength grating coupler. b. SEM images of the grating coupler. Inset: the enlarged view of the subwavelength grating coupler. The simulation and experimental results of subwavelength grating couplers after transfer. c. the holes are not filled with SU-8. d. the holes are filled with SU-8. Red: simulation curve. Blue: experimental results.

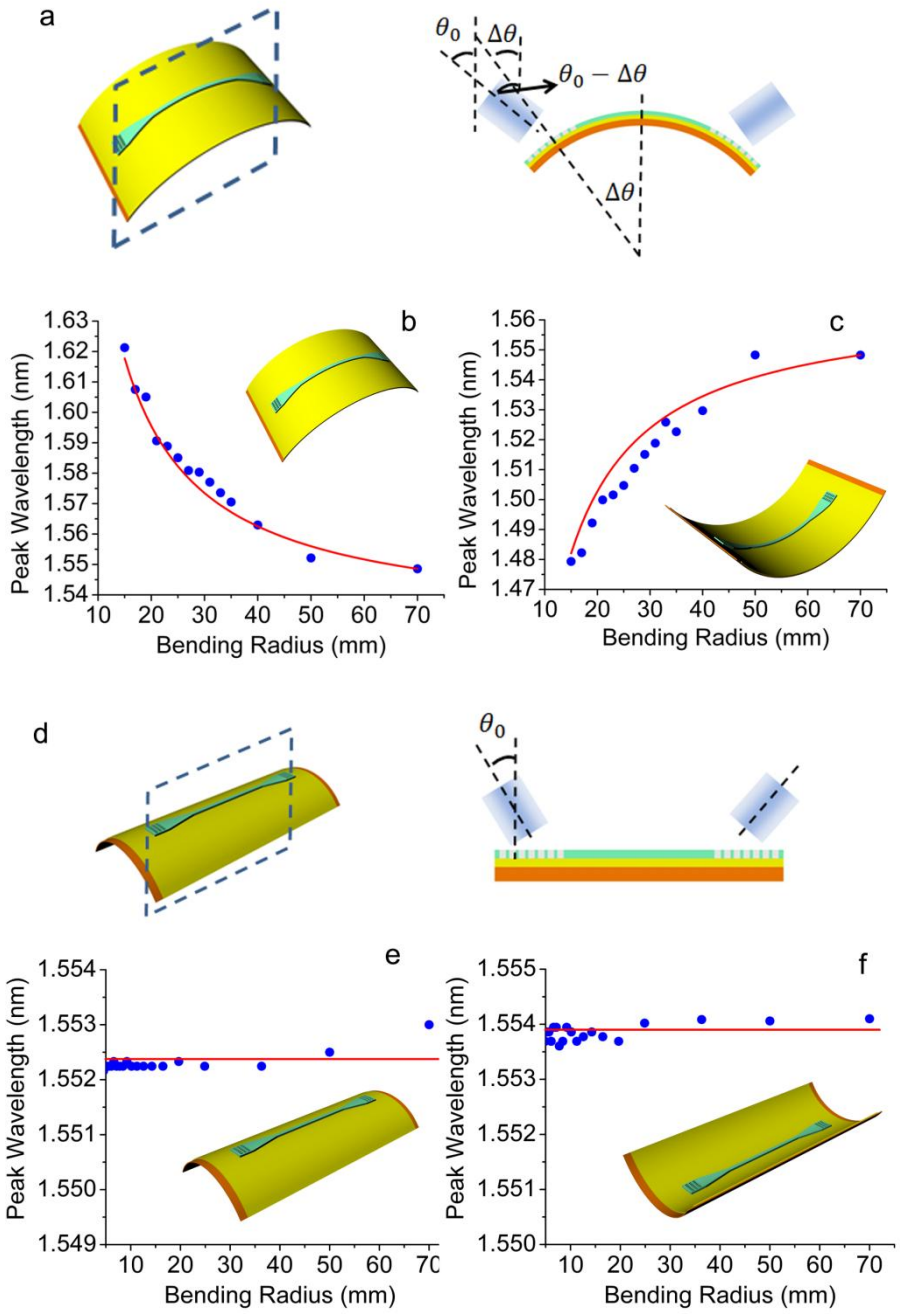

Figure S6

Peak wavelength shift of grating couplers under different bending conditions. a. schematic of the longitudinal bending. b. longitudinal face-out bending. c. longitudinal face-in bending. d. schematic of the transverse bending. e. transverse face-out bending. f. transverse face-in bending.

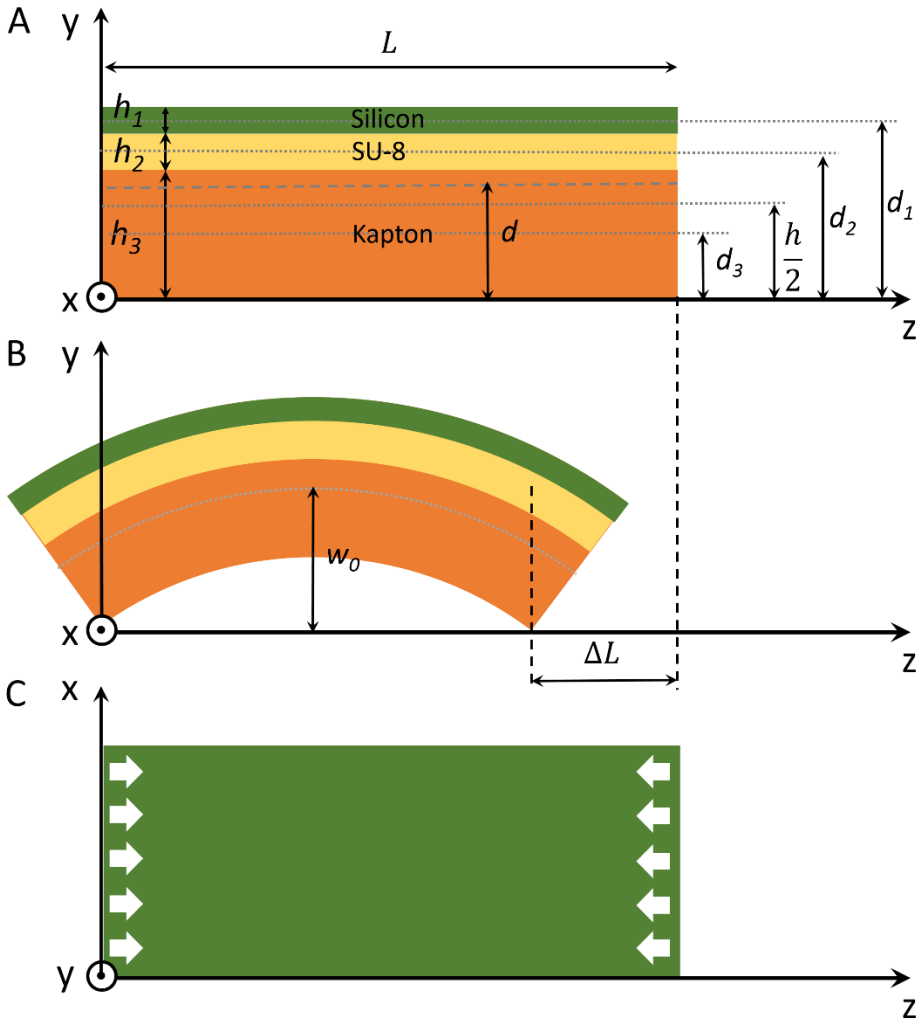

Figure S7
Schematics for the 2D simulation models. (A)(B) The mechanical model in the yz plane. h_i (i=1,2,3)- the thickness of silicon, SU-8, and Kapton; d_i (i=1,2,3)- the position of the middle planes of silicon, SU-8, and Kapton; d- mechanic neutral plane; h- the total thickness of the sample ($h=h_1+h_2+h_3$); (C) The deformation of the device in xz plane is simulated by applying the strain estimated from the bending in yz plane.

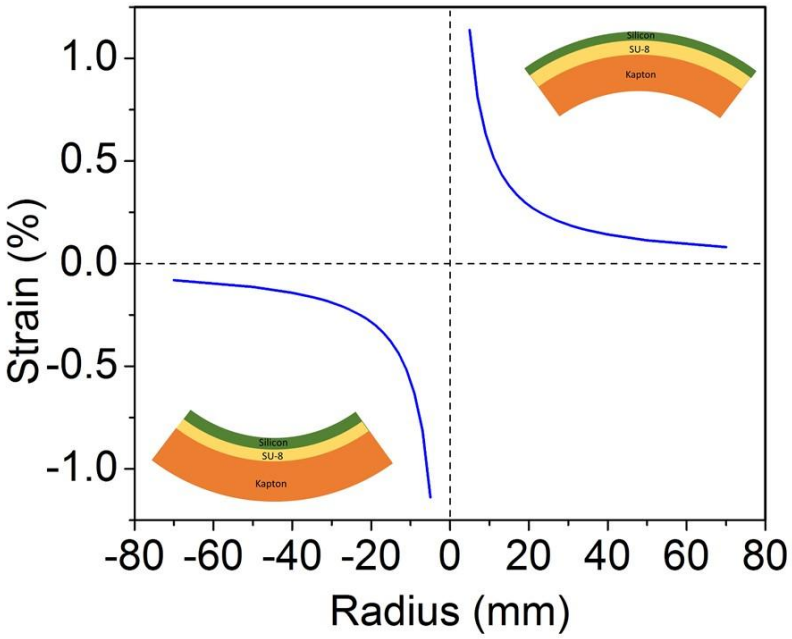

Figure S8
The strain of the silicon nanomembrane in relation to the bending radius. The maximum strain achieved is around 1% for our configuration.

Table S1.

Material characteristics and thickness

Material	Young's Modulus (GPa)	Poisson's Ratio	Thickness (μm)
Si <110>	169	0.28	0.25
Si <100>	130		
SU-8	2	0.22	3
Kapton	2.5	0.34	125

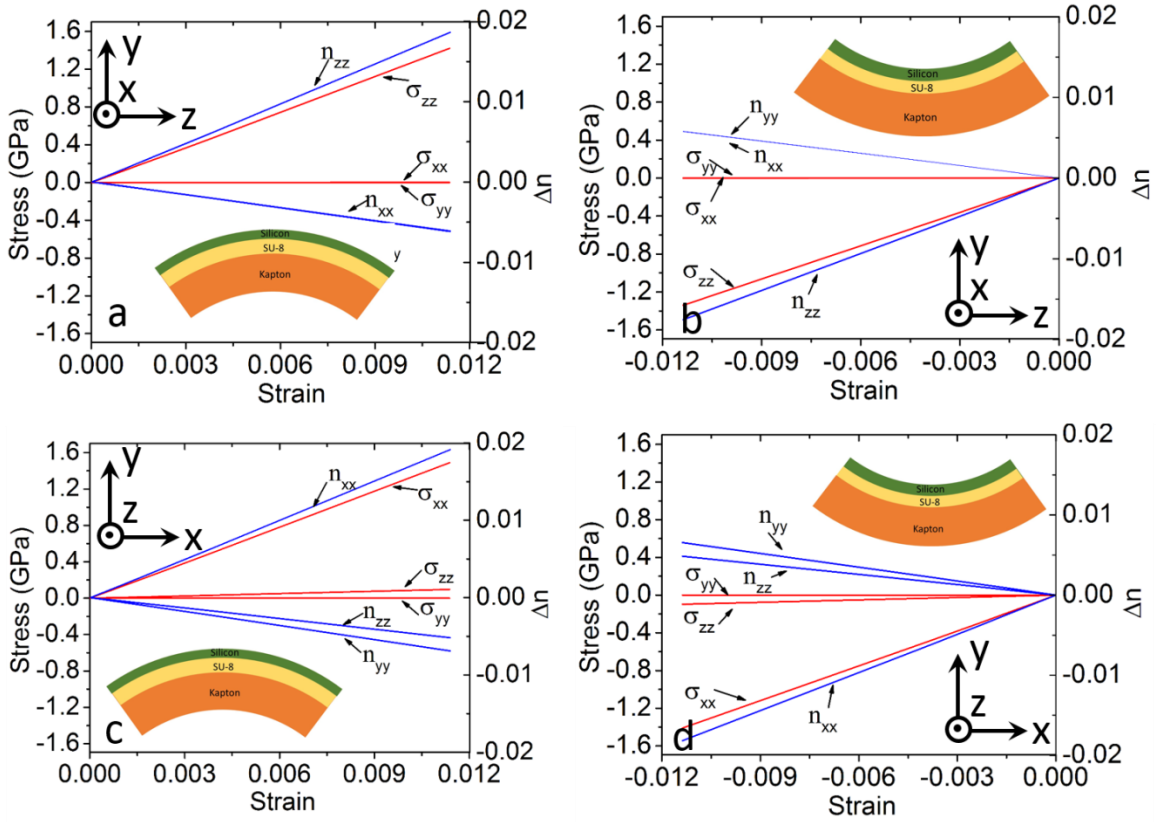

Figure S9.

The averaged stress and the photo-elastic effect induced refractive index variation. a. longitudinal face-out bending. b. transverse face-out bending. c. longitudinal face-in bending. d. transverse face-in bending.

Movie S1

Flexible single-crystal silicon nanomembrane based photonic crystal microcavity

Reference

1. Pfeiffer, K.; Fink, M.; Gruetzner, G.; Bleidiessel, G.; Schulz, H.; Scheer, H. Multistep Profiles by Mix and Match of Nanoimprint and UV Lithography. *Microelectron. Eng.* **2001**, 57–58, 381-387.
2. Santeri, T.; Sami, F. Wafer-Level Bonding of MEMS Structures with SU-8 Epoxy Photoresist. *Phys. Scr., T* **2004**, *114*, 223-226.
3. Madou, M. J. Fundamentals of Microfabrication and Nanotechnology. 3rd ed.; CRC press: 2011.
4. Xu, X. C.; Subbaraman, H.; Hosseini, A.; Lin, C. Y.; Kwong, D.; Chen, R. T. Stamp Printing of Silicon-Nanomembrane-Based Photonic Devices onto Flexible Substrates with a Suspended Configuration. *Opt. Lett.* **2012**, *37*, 1020-1022.
5. Taillaert, D.; Van Laere, F.; Ayre, M.; Bogaerts, W.; Van Thourhout, D.; Bienstman, P.; Baets, R. Grating Couplers for Coupling between Optical Fibers and Nanophotonic Waveguides. *Jpn. J. Appl. Phys.* **2006**, *45*, 6071-6077.
6. Tang, Y. B.; Wang, Z.; Wosinski, L.; Westergren, U.; He, S. L. Highly Efficient Nonuniform Grating Coupler for Silicon-on-Insulator Nanophotonic Circuits. *Opt. Lett.* **2010**, *35*, 1290-1292.
7. Roelkens, G.; Vermeulen, D.; Van Thourhout, D.; Baets, R.; Brision, S.; Lyan, P.; Gautier, P.; Fedeli, J. M. High Efficiency Diffractive Grating Couplers for Interfacing a Single Mode Optical Fiber with a Nanophotonic Silicon-on-Insulator Waveguide Circuit. *Appl. Phys. Lett.* **2008**, *92*, 131101.
8. Xu, X. C.; Subbaraman, H.; Covey, J.; Kwong, D.; Hosseini, A.; Chen, R. T. Complementary Metal-Oxide-Semiconductor Compatible High Efficiency Subwavelength Grating Couplers for Silicon Integrated Photonics. *Appl. Phys. Lett.* **2012**, *101*, 031109.
9. Halir, R.; Cheben, P.; Schmid, J. H.; Ma, R.; Bedard, D.; Janz, S.; Xu, D. X.; Densmore, A.; Lapointe, J.; Molina-Fernandez, I. Continuously Apodized Fiber-to-Chip Surface Grating Coupler with Refractive Index Engineered Subwavelength Structure. *Opt. Lett.* **2010**, *35*, 3243-3245.
10. Chen, X.; Tsang, H. K. Nanoholes Grating Couplers for Coupling between Silicon-on-Insulator Waveguides and Optical Fibers. *IEEE Photon. J.* **2009**, *1*, 184-190.
11. Yeh, P.; Yariv, A.; Hong, C. S. Electromagnetic Propagation in Periodic Stratified Media .1. General Theory. *J. Opt. Soc. Am.* **1977**, *67*, 423-438.
12. Park, S. I.; Ahn, J. H.; Feng, X.; Wang, S. D.; Huang, Y. G.; Rogers, J. A. Theoretical and Experimental Studies of Bending of Inorganic Electronic Materials on Plastic Substrates. *Adv. Funct. Mater.* **2008**, *18*, 2673-2684.
13. Timoshenko, S. P.; Gere, J. M. Theory of Elastic Stability. 2nd ed.; Dover Publications: 2009.
14. Bareisis, J. Stiffness and Strength of Multilayer Beams. *J Compos Mater* **2006**, *40*, 515-531.
15. Yang, S. X.; Lu, N. S. Gauge Factor and Stretchability of Silicon-on-Polymer Strain Gauges. *Sensors* **2013**, *13*, 8577-8594.
16. Huang, M. Stress Effects on the Performance of Optical Waveguides. *Int. J. Solids. Struct.* **2003**, *40*, 1615-1632.
17. Fan, S. Photonic Crystals: Theory and Device Applications. Massachusetts Institute of Technology, 1997.

18. Chen, Y.; Li, H.; Li, M. Flexible and Tunable Silicon Photonic Circuits on Plastic Substrates. *Sci Rep* **2012**, *2*, 622.
19. Sadd, M. H. Elasticity Theory, Applications, and Numerics. 2nd ed.; Academic Press: 2009.